This manuscript has been authored by UT-Battelle, LLC under Contract No. DE-AC05-00OR22725 with the U.S. Department of Energy. The United States Government retains and the publisher, by accepting the article for publication, acknowledges that the United States Government retains a non-exclusive, paid-up, irrevocable, world-wide license to publish or reproduce the published form of this manuscript, or allow others to do so, for United States Government purposes. The Department of Energy will provide public access to these results of federally sponsored research in accordance with the DOE Public Access Plan (http://energy.gov/downloads/doe-public-access-plan).

Time-Resolved Electrical Scanning Probe Microscopy of Layered Perovskites Reveals Spatial Variations in Photoinduced Ionic and Electronic Carrier Motion

R. Giridharagopal,[1] J. T. Precht,[1] S. Jariwala,[1] L. Collins,[2] S. Jesse,[2] S. V. Kalinin,[2] D. S. Ginger[1]*

[1] Department of Chemistry, University of Washington, Seattle, WA 98195

[2]Center for Nanophase Materials Science, Oak Ridge National Lab, Oak Ridge, TN 37830

*Corresponding Author: dginger@uw.edu

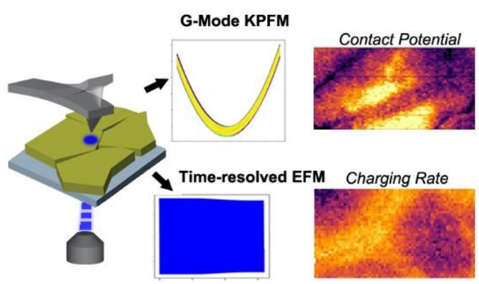

TABLE OF CONTENTS GRAPHIC

Keywords: layered perovskites, time-resolved electrostatic force microscopy, G-Mode, Kelvin probe force microscopy

ABSTRACT

We study light-induced dynamics in thin films comprising Ruddlesden-Popper phases of the layered 2D perovskite $(C_4H_9NH_3)_2PbI_4$ (BAPI). We probe ionic and electronic carrier dynamics using two complementary scanning probe methods, time-resolved G-mode Kelvin probe force microscopy (G-KPFM) and fast free time-resolved electrostatic force microscopy (FF-trEFM), as a function of position, time, and illumination. We show that the average surface photovoltage sign is dominated by the band bending at the buried perovskite-substrate interface. However, the film exhibits substantial variations in the spatial and temporal response of the photovoltage. Under illumination, the photovoltage equilibrates over hundreds of microseconds, a timescale associated with ionic motion and trapped electronic carriers. Surprisingly, we observe that the surface photovoltage of the 2D grain centers evolves more rapidly in time than at the grain boundaries. We propose that the slower evolution at grain boundaries is due to a combination of ion migration occurring between PbI_4 planes, as well as electronic carriers traversing grain boundary traps, thereby changing the time-dependent band unbending at grain boundaries. These results provide a model for the photoinduced dynamics in 2D perovskites and are a useful basis for interpreting photovoltage dynamics on hybrid 2D/3D structures.

Organic-inorganic hybrid halide perovskites are widely-studied materials for thin film optoelectronics, including photovoltaics and light-emitting diodes.[1-4] Conventionally, films for photovoltaic applications have been made from the typical 3D perovskite ABX_3, where A = a monovalent (often organic) cation, B = a divalent (typically inorganic, Pb^{2+}) cation, and X = a monovalent halide anion; the canonical halide perovskite structure used for solar cells being $CH_3NH_3PbI_3$ (MAPI). However, ion motion, stability, and defect formation are factors that still need to be understood and controlled.[5-7]

In an effort to improve moisture-related stability issues that can affect 3D perovskites, several groups have reported the use of reduced dimensional phases, including 2D layered

Ruddlesden-Popper systems.[8-14] Lower-dimensional perovskite materials also exhibit attractive benefits in light-emitting applications[15-19] given their high (100-300 meV)[20-24] exciton-binding energies compared to the small ~7 meV binding energies of conventional perovskites.[25] Recent efforts have shown improvements in the performance in these materials, in particular with purported 2D/3D combinations that tune the benefits of 3D perovskites with enhanced stability due to the spacer cations.[9, 11, 12, 16, 26]

While the hydrophobic surfaces and general reduction in water absorption likely play a role in the longer lifetimes of the 2D perovskites,[8, 12] the exact origin of their increased stability, yet mixed performance, compared to their 3D parent structures is still unclear. Ion motion, perhaps dominated by grain boundaries, perhaps by halide vacancies or intrinsic defects,[6] is currently believed to be a major source of instability in 3D hybrid perovskites and their derivative structures.[5, 6, 27] In addition to being the likely source of hysteresis in many devices, ion motion can, in conjunction with charge injection, lead to formation of non-radiative defect centers,[28] and has been proposed as a dominant source of loss and instability threatening the long-term success of hybrid perovskite-based technologies.[27, 29]

In this context, one hypothesis put forward to explain the improved stability of the layered 2D hybrid perovskites relative to their 3D analogs is a reduction in ion mobility in the 2D phase due to the planes of (typically) hydrophobic aliphatic chains parallel to the layering axis.[30, 31] On the other hand, ion motion across the layered planes has been demonstrated, even in single crystals.[32] In order to better understand these phenomena, we study local photoinduced ion motion in 2D Ruddlesden-Popper phases.

Ruddlesden-Popper layered films are formed by using bulky organic cations that cannot intercalate within the perovskite layers. One common example of Ruddlesden-Popper halide perovskites occurs with the use of butylammonium cations in butylammonium/methylammonium lead iodide, which has the general form $(C_4H_9NH_3)_2(CH_3NH_3)_{n-1}Pb_nI_{3n+1}$. In the limit of *n=1* these films consist of a single PbI_4 layer separated by butylammonium cations (**Fig. 1A**) (BAPI). Single layer films like BAPI provide a limiting case from which processing can be optimized to improve, for instance, luminescence quantum yield[15] in LEDs or to tailor cations to enhance PCE in solar cells.[33] Furthermore, while early reports tended to focus on spatially-averaged photoluminescence properties,[34, 35] the more recent trend towards mixed 2D/3D systems has renewed interest in understanding nanoscale electronic structure-function relationships. Beyond those systems, the wide tunability of 2D systems has encouraged intense research in studying their basic properties[14] and in other applications like transistors.[36, 37]

Here, we show that layered *n=1* BAPI films exhibit highly heterogeneous dynamics across multiple timescales in response to photoexcitation, with grain boundaries exhibiting slower photoinduced charge buildup relative to grain interiors. We use a combination of two data-intensive electrical scanning probe methods, time-resolved EFM (FF-trEFM)[38-44] and General-Mode KPFM (G-KPFM), to locally probe photoinduced dynamics at microsecond timescales. We propose that these dynamics are related to a combination of ion motion and relatively slow carrier motion through energetic traps at these boundaries, given the ~hundreds of microseconds timescales observed. Together, these data also demonstrate the utility of modern "big data" processing methods for scanning probe information.[45]

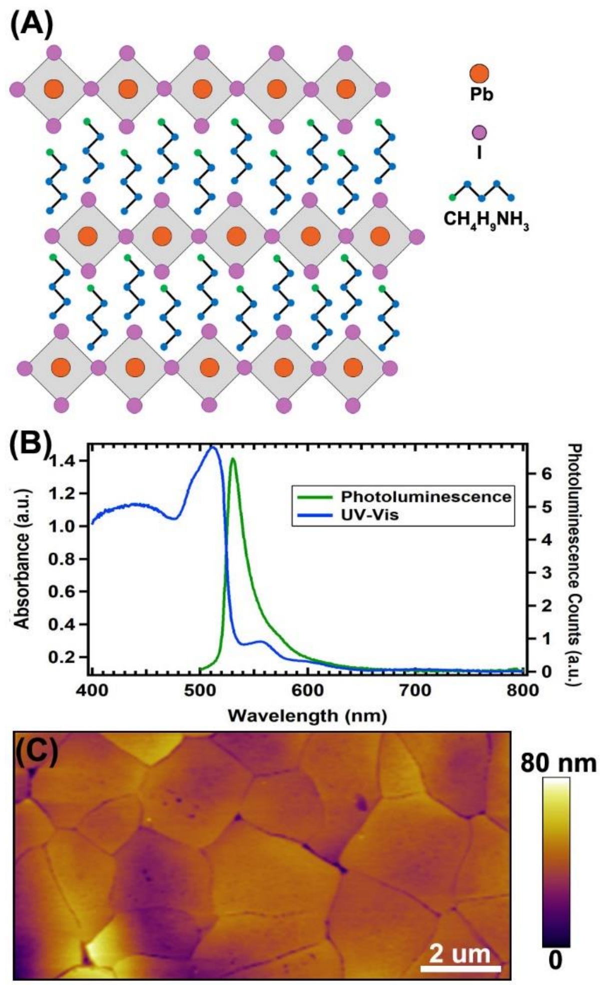

Fig. 1. Representative schematic and structure of $(C_4H_9NH_3)_2PbI_4$ (BAPI) (A) Structure of the 2D Ruddlesden-Popper BAPI system, of general form $(C_4H_9NH_3)_2(CH_3NH_3)_{n-1}Pb_nI_{3n+1}$ where n=1 here. (B) Representative UV-Vis and photoluminescence spectra of BAPI films. (C) Representative topography of BAPI on ITO showing grains of several microns.

RESULTS AND DISCUSSION

We study BAPI, $(BA)_2(MA)_{n-1}Pb_nI_{3n+1}$ with $n=1$, as the simplest representative member of the layered Ruddlesden-Popper lead halide perovskites with butylammonium cations. Fig. 1 shows the crystal structure (**Fig. 1A**), optical characterization (**Fig. 1B**) (UV-Vis and PL), and AFM topography (**Fig. 1C**) of the BAPI (n=1) films typical of those we used for this study. The data in Fig. 1 are characteristic of BAPI thin films, and consistent with the reported bandgap (~2.24 eV[8, 46]) (**Fig. 1B**) as well as exciton absorption at ~510 nm reported previously[8, 33, 46] that is *n*-dependent,[47] though not layer-dependent.[48] BAPI films on ITO tend to form grains with scale of several microns, **(Fig. 1C)** with the PbI_4 planes parallel to the surface,[8] and a roughness in the grains of ~15 nm with some voids between crystals. On TiO_2 we observe similar structures with albeit slightly smaller crystal sizes (~1-2 μm) (**Fig. S1A**). Using the preparation described in the Methods section, we yield films with ~500 nm thickness and grains of >1 μm diameter. X-ray diffraction data (**Fig. S1**) are consistent with those results found in similar *n*=1 materials for the (00l) locations.[8, 49, 50]

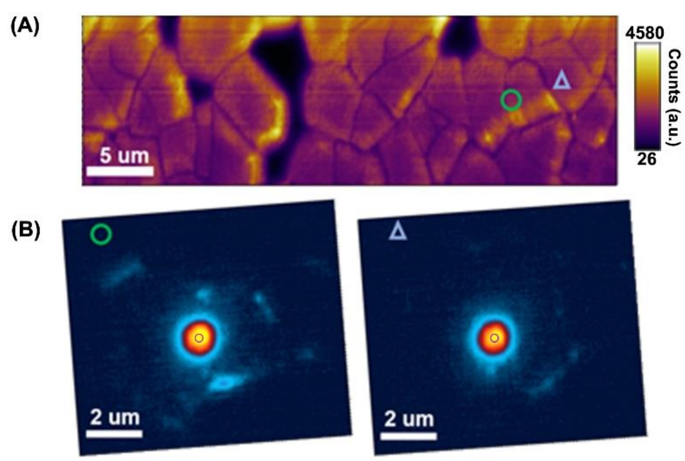

Fig. 2. Photoluminescence mapping of BAPI films. (A) Confocal photoluminescence mapping with λ=470 nm (9 μJ/cm^2 per pulse) excitation over a representative BAPI film on glass. (B) Local excitation and widefield collection of photoluminescence. Here, the lifetime is short enough (~1 ns, **Fig. S2, S3**) that only the area adjacent the laser spot is observed +/- ~1 μm, in contrast to the case with 3D perovskites. The beam diameter, measured as ~300 nm, is shown as a red circle in the center of each excitation spot. The intensity variation in (A) is due to photodegradation over

the course of the scan under high fluence, which is common for the n=1 films even when imaged in dry N2.

We first study these films with conventional confocal photoluminescence (PL). These images show that that the emission properties of the film are heterogeneous, with brighter areas exhibiting greater PL intensity (see also **Fig. 2**).[51] However, the short lifetime of <~1 ns across the image (**Fig. S3**) due to the high exciton binding energy[22, 34] results in <100 nm diffusion lengths.[35,52] As a result, PL images taken with confocal excitation and widefield detection (**Fig. 2B**) show primarily the ~300 nm wide confocal laser spot itself with ~700 nm diffusion into the surrounding grain, yet little of the grain-dominated behavior observed on films of 3D perovskites.[53] In contrast to 3D perovskites which generate free carriers with long diffusion lengths,[54] the recombination and emission occurs almost entirely within the diffraction-limited laser spot, with some edge-dependent light-scattering effects depending on the grain (**Fig. S2**).

Next, to better understand grain-dependent dynamics in these systems, we turn to scanning probe microscopy (SPM) methods. We first use conventional KPFM to study these materials (**Fig. 3**). Briefly, in KPFM an AC bias voltage is applied between the tip and a substrate. A DC nulling potential is applied to the tip to cancel any oscillation amplitude at this particular AC frequency, and the value of the nulling potential is then the "contact potential difference" (CPD). Here, we use the convention where CPD is defined as $(\Phi_{Tip} - \Phi_{sample})/e$, Φ being the work function, and the CPD is equal to the sign of the bias applied to the tip. That is, if the CPD is more positive, it indicates a shallower work function (closer to vacuum, or more n-type for a semiconductor); a more negative CPD corresponds to a deeper work function.

Fig. 3 shows a KPFM image on a BAPI film taken under dry nitrogen. Compared to the dark CPD (**Fig. 3B**), under illumination (**Fig. 3C**) BAPI shows a more negative CPD everywhere.

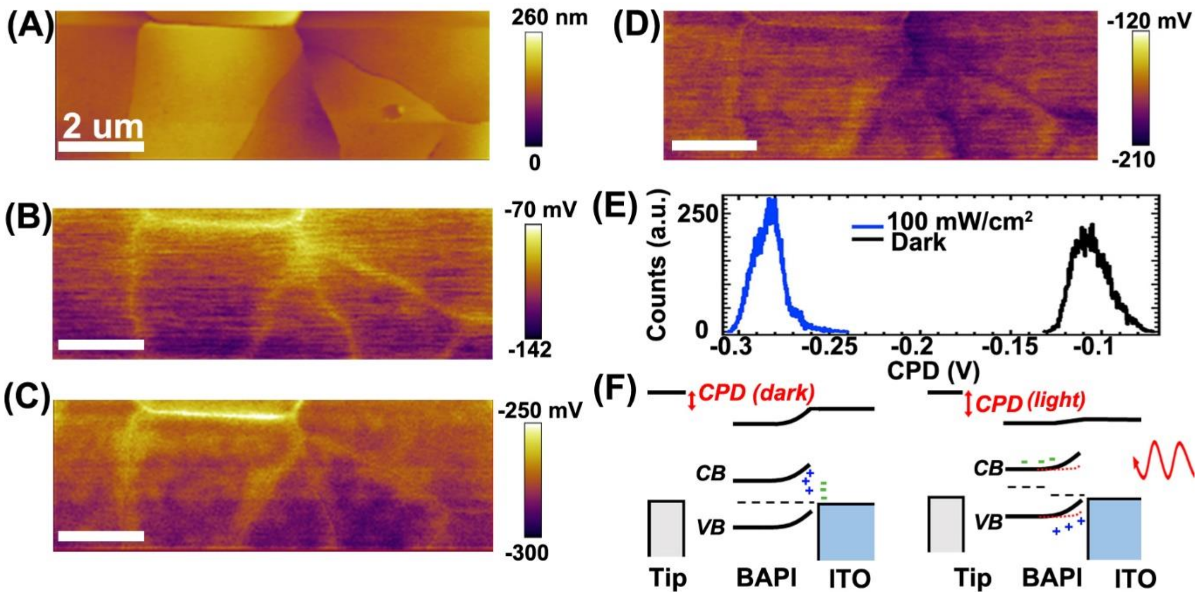

Fig. 3. Surface photovoltage of a $(C_4H_9NH_3)_2PbI_4$ (BAPI) film. (A) Topography. (B) Dark KPFM and (C) KPFM under ~150 mW/cm^2 455 nm illumination. (D) Surface photovoltage calculated as the pixel-wise difference of (B) and (C). (E) Histogram of the contact potential difference (CPD) showing a negative surface photovoltage. (F) Band diagram showing flattening of the band at the BAPI-ITO contact under illumination.

Interpreting surface photovoltage data can be complicated,[55] particularly in mixed ionic/electronic conductors like perovskites.[56] In this case, ITO has a work function of ~4.7 to 5 eV depending on preparation.[57, 58] While previous reports have measured a valence band maximum of BAPI at ~4.6 eV,[8, 33, 46] Silver, et al. recently reported a valence band minimum of -5.8 eV.[59] We use calibrated KPFM compared to freshly-cleaved graphite to confirm a value closer to -5.8 eV in our samples here (see **Fig. S4** and related discussion).". As a result, when BAPI is deposited on ITO, electrons should flow from BAPI into the ITO until the Fermi levels are equilibrated. The resulting charge transfer from the perovskite to the ITO leads to band bending at the perovskite/ITO interface as depicted in (**Fig. 3F**). Under illumination, the built-in field preferentially pushes any photogenerated electrons away from the BAPI-ITO junction and photogenerated holes towards the junction, thus reducing the built-in potential barrier and flattening the bands. In SPV measurements on a semiconductor, the nature of the CPD shift under illumination can be influenced by both surface charge/band bending and the electronic interface with the back contact. In our experiments here, the overall ~ -200 mV SPV shift is consistent with the dominant effect being a photoinduced reduction in band bending at the buried BAPI/ITO contact. To test this hypothesis, we also performed SPV experiments on BAPI grown on TiO_2 (see **Fig. S5** in SI for data on TiO2). TiO_2 grown by the method used here typically has a work function of 4.0 eV,[60] resulting in the opposite sign band bending at the perovskite/TiO_2 contact compared to the perovskite ITO contact. We therefore expect the SPV to exhibit an opposite sign on the BAPI/TiO_2 samples if our hypothesis that photoinduced flattening of the back surface band bending is the largest contributor to the average SPV signal. **Fig. S5** shows that the BAPI/TiO_2 samples indeed show a net positive SPV. Because the surface photovoltage has an opposite sign on ITO (negative), and TiO_2 (positive) substrates due to the different energetics at the perovskite-contact interface,[61, 62] we thus conclude that our measured SPV data are consistent with photoinduced unbending of the bands at the electrode/perovskite interface.[55]

Importantly however, in all images the difference between the illuminated and dark CPD values (the surface photovoltage (SPV), **Fig. 3D**) show that the photovoltage is more negative at the grain boundaries on *both* the ITO and TiO_2 substrates. This effect is evident in the separate CPD histograms (**Fig. 3E**) where the shapes of the distributions change by more than a simple offset due to the illumination; that is, the system changes non-uniformly under illumination. This contrast is important because if the photovoltage was only from band unbending at the back contact, then the *magnitude* would be greater at grain boundaries on both TiO_2 and ITO but would be opposite sign on TiO_2 (more positive). However, the grain boundaries show more negative photovoltage (more p-type character) for both substrate materials. These data show that the static photovoltage contrast is a combination of both buried contacts and surface effects, with the perovskite grain boundaries becoming on average, more positively charged than the bulk following illumination.

Photovoltage Dynamics with G-KPFM:

Having probed the static surface photovoltage and its substrate-dependent sign, we now explore the dynamic changes in surface photovoltage that occur on sub-millisecond timescales as the sample equilibrates under illumination. While heterodyne KPFM can probe perovskite dynamics on the timescale of seconds or milliseconds,[63-67] and dissipation methods can probe single pixels with microsecond,[68] we seek to probe the timescale over which the surface photovoltage evolves on sub-millisecond scales, and to explore if that timescale varies with the local film structure at or away from a grain boundary. It is important to have methods that span a wide range of timescales from seconds down to sub-millisecond regimes. For sub-millisecond effects, carrier mobilities in perovskites tend to be high (even in n=1) and can even be sub-microsecond. For some ionic species, slower motion can occur in the realm of milliseconds given the different mobilities for the various ions in the film, and thus millisecond-resolution probes are useful for slower ion dynamics. Longer timescale effects can include irreversible phenomena, such as charging or photobrightening effects, that occur on the timescale of seconds or longer To achieve this time-resolution goal, we first probe SPV dynamics *via* G-KPFM (**Fig. 4A, schematic)**, a "big data" approach to SPM described in recent reports.[69-72]

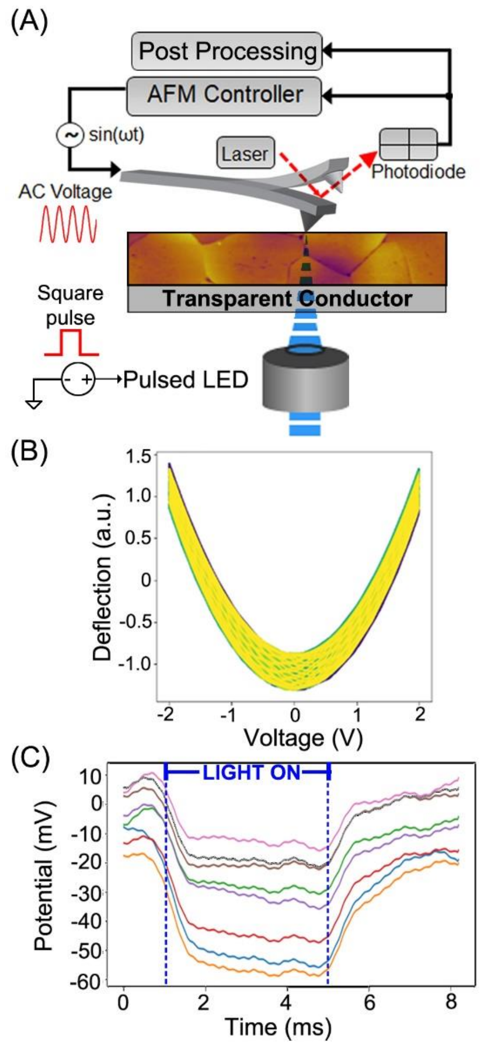

Fig. 4. Schematic and example CPD. (A) Instrumentation schematic showing AC voltage applied between the tip and the substrate, with a voltage step applied to turn on an LED in a controlled time window at each pixel. The resulting photodiode response is digitized and processed. (B) The filtered photodiode signal plotted against the AC voltage waveform exhibits a parabolic shape for several pixels. Fitting a second order polynomial yields the voltage corresponding to the peak at

each time step, corresponding to the contact potential. (C) The potential is plotted *versus* time for several representative pixels. The period where the light is on is, in this case, from 1 to 5 ms.

In G-KPFM we apply an AC voltage signal to the tip that is tuned to the resonance of the cantilever, which allows us to measure the deflection vs. AC voltage multiple times within a single cantilever oscillation and extract the CPD (**Fig. 4B**), in some cases, in less time than a single cantilever oscillation. Importantly, this process is performed without the tip voltage-feedback loop, distinguishing it from classical KPFM schemes which null the potential.[73] At each pixel, the light is turned on for a fixed duration (typically 4 ms here). We then can extract the CPD during the dark and illuminated case to yield the SPV. After de-noising (see Methods section) we fit exponential decays to the CPD vs. time traces to extract local time constants (**Fig. 4C)**.

Fig. 5A-E shows G-KPFM images on BAPI films on ITO illuminated with a 455 nm LED at ~60 mW/cm^2; this intensity is many orders of magnitude less than the high fluence in the confocal image (**Fig. 2**). The CPD shifts to a more negative value (more positively charged sample) during illumination, as was shown in the static SPV images (**Fig. 3**), consistent with electron transfer to the ITO and photoinduced hole accumulation on the perovskite. However, we can now resolve the photovoltage shift in time, and each pixel in **Fig. 5** contains time-resolved information, like the data in **Fig. 4C.** We plot the fitted time constant in **Fig. 5F** and **5G** to generate CPD "charging" and "discharging" maps. The charging and discharging maps exhibit similar spatial contrast to each other, with the CPD near grain boundaries changing more slowly than the grain interiors. The discharging time constants here are ~2X longer than the photoinduced charging time constants. Individual CPD traces are shown in **Fig. S7**, and we attribute the lateral variation to possible variations in the contact to ITO. Consecutive images of the same area show similar CPD values and time constants as well (see SI) and do not reveal strong charging effects (**Fig. S10**).To exclude topographic artifacts as the source of contrast, we can also compare the resulting data against the gradient (**Fig. S12**).

Assuming the ~200 μs time-evolution of the ~60 mV photovoltage results from drift of charged species in the surface potential and a thickness of ~500 nm, we estimate an average mobility of the charges responsible for the photoinduced shifts to be on the order of ~10^{-5} $cm^2V^{-1}s^{-1}$. This value is 100,000 times smaller than the carrier mobility of ~0.5 - 1 $cm^2V^{-1}s^{-1}$ that have been reported in-plane.[52, 74] On the other hand, assuming a dominant ion mobility of 10^{-7} to 10^{-6} cm^2/V-s (comparable to iodide in the 3D halide perovskites[75]), these hundreds of microsecond time constants would correspond to ion transport lengths ($L^2/\tau = \mu k_B T/q$) of ~500 nm to 1 μm- which are comparable to the feature sizes (grain boundaries and film thickness) observed in our current films. We thus conclude that these measured G-KPFM time constants, on the order of hundreds of microseconds, would appear to be more consistent with ion motion. However, the slow motion of deeply trapped carriers, could also be consistent with these timescales. While it has been argued that ion migration should be inhibited by the organic cation spacer layer,[31] we note that Br^- motion perpendicular to the perovskite layer in $PbBr_4$ systems has been observed in recent reports focusing on resistive switching in *n=1* type materials, albeit at high fields.[32, 76]

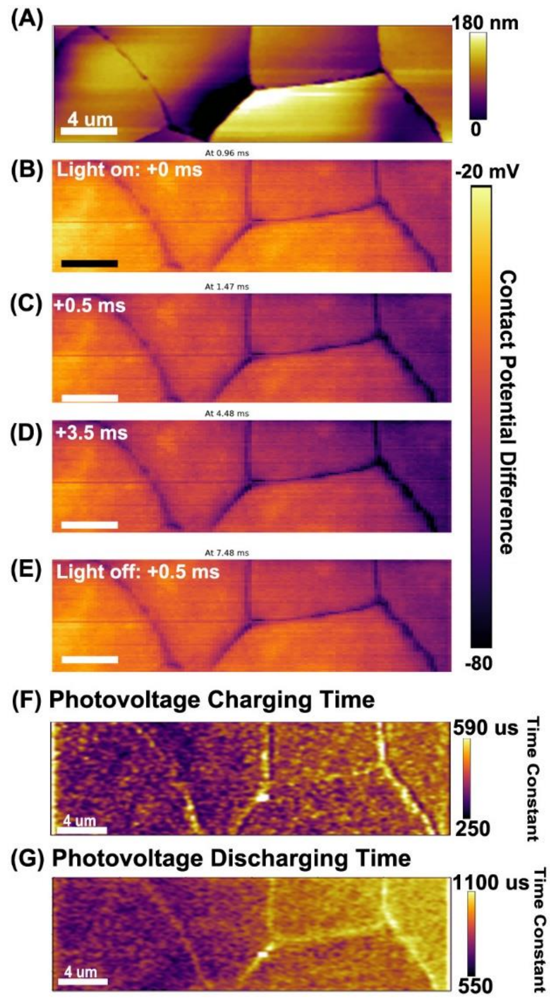

Fig. 5. Time-Resolved G-KPFM on BAPI films. (A) Topography and (B-E) Time slices of contact potential images on the same location showing the evolution of contact potential over the image. (F) The reconstructed CPD charging time constant and the (G) discharging time constant over the image. Illumination source is 455 nm and ~60 mW/cm^2.

From the charging and discharging images, we observe that the surface potential is consistently more negative adjacent to grain boundaries on BAPI. To confirm this quantitatively, in **Fig. 6A-B** we show a contact potential difference image on BAPI as a function of distance to nearest grain boundary (**Fig. 6C**). We apply unsupervised learning *via* *k*-means clustering to segment the G-KPFM data into three sets of pixels. We then plot the average contact potential as a function of distance to the nearest grain edge pixel (see **Fig. S11** and related discussion for details). Similar clustering has been used in recent scanning probe microscopy studies,[70, 77] including three-dimensional G-KPFM surface photovoltage measurements.[69] The scatter plot (**Fig. 6C**) shows quantitatively that as the distance to nearest grain boundary increases (*i.e.* more towards the center of a given grain) the CPD also becomes more positive (more n-type/less p-type). We overlay the clustering pixels corresponding to these three feature sets in **Fig. 6D.** In addition, we consistently observe that the potential drop near the grain boundaries becomes *narrower* under illumination, shifting from ~1 um wide in the dark, to ~750 nm wide under illumination (**Fig. S8, S9)**.

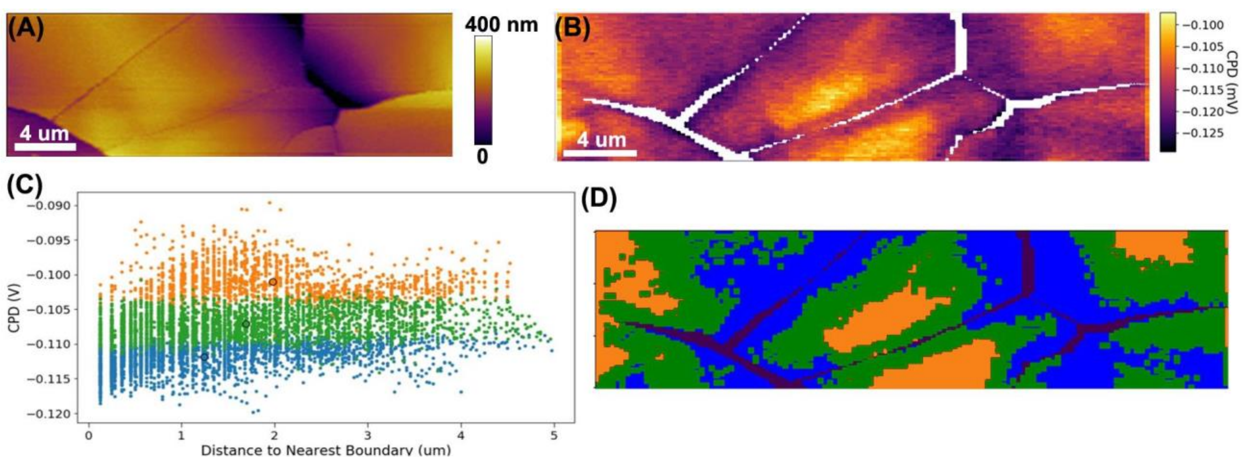

Fig. 6. Clustering spatial dependence of contact potential variations under illumination. (A) Topography and (B) CPD of a BAPI film (under 455 nm illumination, ~150 mW/cm^2), with pixels defining the grain boundaries masked off for clustering. (C) CPD of the pixels plotted *versus* distance to the nearest grain boundary pixel, using the mask in (B) to define the grain boundaries based on the amplitude image. The colors correspond to regions defined by unsupervised *k-means* clustering of the G-KPFM data at each pixel, thereby quantifiably categorizing the data into

regions. These data show that as the distance to the nearest grain boundary increases (towards center of the grain) the CPD tends to increase, as indicated by the centroids of each cluster depicted as a solid circle. (D) Clustering of the 4-dimensional data (x, y, CPD, time) *via k-means* confirms these findings, with the clusters lying across contours of potential. These data show that the time series information are reflective of the spatial component of the CPD data relative to the grain boundary position, and they show that the average shifts to higher potentials at grain interiors.

Time-Resolved EFM Dynamics:

The time constants we measure with time resolved G-KPFM are consistent with ion motion, electronic carriers moving in a manifold of traps, or a mixture of both, occurring on timescales of ~100-300 μs. Since BAPI is a mixed conductor it therefore could reflect dynamics from both ions and electronic carriers, with characteristic times faster than is measured in our G-KPFM data. To look for signals faster than could be resolved with G-KPFM data, we next extract fast dynamics using fast free time-resolved electrostatic force microscopy (FF-trEFM). FF-trEFM, like the newer G-KPFM method, is also a feedback free approach that involves digitizing the entire free response of the cantilever following a perturbation to recover fast dynamics. FF-trEFM analyzes the time-dependent frequency shift of the cantilever following a transient excitation (in this case, an LED pulse) to discriminate between sub-microsecond transient phenomena[39] or even sub-100 ns transients as long as the phase of the excitation is controlled precisely.[78, 79] In FF-trEFM it is possible to see the combination of time constants, such as combination of fast electronic and slow ionic characteristic processes, as a single effective time (**Fig. S18**).

Here, we use FF-trEFM to probe similar films to those in the G-KPFM data. As shown in **Fig. 7**, consistent with the G-KPFM data, FF-trEFM also shows generally faster charging at grain interiors with slower photoinduced charging near grain boundaries. The experimental data correspond to actual time constants of ~30 to 70 μs based on simulations of the calibrated cantilever (**Fig. S13**). We observe two key features: 1) charging is slower at grain boundaries (**Fig. 7B)** 2) the magnitude of the frequency shift is greater at grain edges (**Fig. 7C**), which is consistent with larger surface photovoltage shifts at grain boundaries although the shift can be prone to topographic crosstalk more so than the charging rate or the G-KPFM.[38] Unsupervised clustering confirms that the time constants at grain interiors indeed tend to shorter (faster charging) (**Fig S17)**. In this case, the average t_{FP} decreases by ~15 us from regions associated with grain boundaries compared to regions associated with grain interiors. We can use the frequency shift, which is generally related to the total photogenerated charge, to show that the charging rate differences from center to edge are not due to changes in absorption from scattering near grain boundary edges.

These data are consistent with the G-KPFM approach in terms of the charging rates as a function of grain boundary position. The comparatively faster time constants being measured by FF-trEFM might be interpreted in a few ways: 1) variations in photocurrent generation rate as in systems without ionic carriers;[39] 2) ionic and electronic carrier transport times that are faster in FF-trEFM compared to G-KPFM due to different instrument response and applied fields between FF-trEFM and G-KPFM. Additionally, we note that much higher light intensities than used here are required to generate detectable electronic currents in these films (as shown in photoconductive AFM **Fig. S19**), particularly at grain centers

We thus propose that differences in the electrical excitation and response profiles between the technique of G-KPFM and FF-trEFM can account for the quantitative differences in kinetics. Notably, in FF-trEFM we apply a DC field during illumination, compared to the ~70 kHz AC field during G-KPFM. Since changing the voltage from +5 V (**Fig. S15-S16)** to +7 V (**Fig. 7**) results in slightly faster time constants, and since the ionic response is likely characterized by a range of relaxation times, it seems plausible that the square voltage pulse and AC oscillations sample slightly different weighted portions of the ionic response function. A further difference is in fitting the functional form of the electrostatic force *versus* voltage (G-KPFM) compared to fitting the cantilever relaxation (FF-trEFM), and thus they arrive at electrical information by focusing on different dynamic analyses.

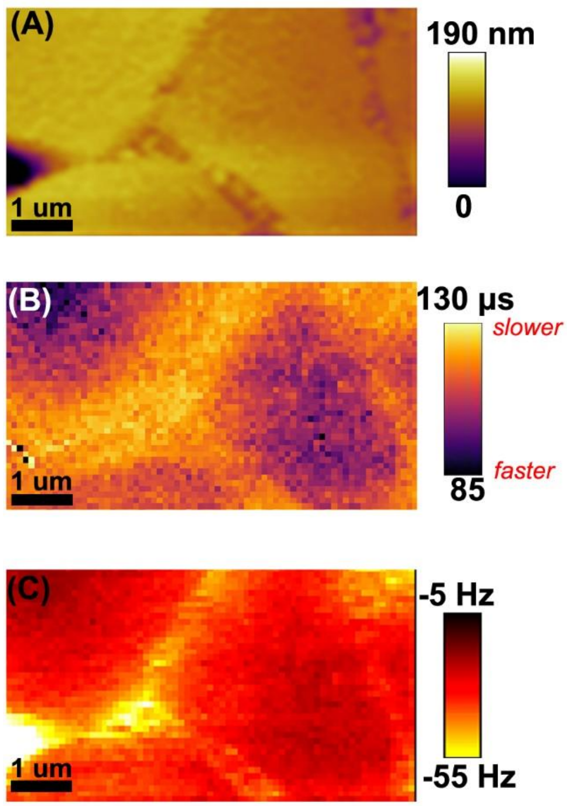

Fig. 7. Fast free time-resolved electrostatic force microscopy (FF-trEFM) on BAPI. (A) Topography, (B) FF-trEFM time constant, and (C) FF-trEFM frequency shift images under 455 nm illumination (~100 mW/cm^2) and V_{tip}= +7 V. Brighter regions exhibit slower charging in (B) and greater total charge (C). Regions adjacent grain boundaries exhibit slower charging and are therefore consistent with the G-KPFM image data.

We take these two dynamic techniques' data together to propose a possible mechanism where ion migration and trap-mediated transport would result in grain boundaries with seemingly slower time constants (see schematic in **Fig. S20)** but larger net photovoltage. As cast, BAPI surfaces contain acceptor-type iodine vacancies but otherwise little inherent doping.[80] Under illumination, photogenerated excitons separate at the BAPI/ITO interface or BAPI surface states,[81] which we observe using photoconductive AFM in **Fig. S19** as has been used on conventional MAPI films.[82] The built-in field from band bending drives holes toward the top surface and reduce band bending. At grain boundaries, the band bending in the dark is less than at grain interiors based on the dark CPD images (**Fig. 2**), implying fewer acceptor-type vacancies. From previous perovskite studies it is thought that free electrons trapped in positively-charged vacancies create an electric field that can induce ion motion,[27] in this case between adjacent planes.[32] In these data, we propose that this effect from trapping induces ion motion, thereby changing the acceptor-type vacancy population while under illumination. As a result, the total band unbending ends up greater at grain boundaries (larger surface photovoltage and greater FF-trEFM frequency shift), while the slower time constant is due to the initially lower screening potential in the dark. Another possibility could be that electronic carriers relax more slowly at grain boundaries in the presence of multiple barriers and a more complex energy landscape. The timescales measured by G-KPFM (sub-millisecond) and FF-trEFM (~100 us or less) indicate a slower phenomenon than free carriers. In this case the carrier mobility at grain boundaries would need to be on the order of 10^{-4} $cm^2V^{-1}s^{-1}$, which is lower than the 0.5 $cm^2V^{-1}s^{-1}$ for n=1 BAPI[74], thus suggesting a slower effect such as trap-mediated carrier transport at grain boundaries.

CONCLUSIONS

In summary, we find that layered perovskites of $(C_4H_9NH_3)_2PbI_4$ (BAPI) exhibit heterogeneous optoelectronic properties using confocal PL and two dynamic AFM methods, G-Mode KPFM and time-resolved EFM. Surprisingly, these methods appear to show that BAPI films exhibit faster surface charge buildup in grain centers rather than at grain boundaries, possibly due to a mixture of ionic and trap-mediated electronic transport. In G-KPFM, this effect happens with timescales on the order of < ~500 μs. In FF-trEFM, which in principle can achieve sub-microsecond time resolution, we also see qualitatively similar behavior where grain boundaries exhibit slower response, with response times we estimate at ~70-100 μs. We propose that this effect is dominated by a change in acceptor-type vacancies and associated screening under illumination due to the generation of photoinduced field that occurs primarily at grain boundaries, along with a higher density of traps at the grain boundaries resulting in slower electronic charging rates. In addition to advancing the use of new SPM methods, especially for energy applications,[83] this study also provides insight into photoinduced ion motion in a model 2D perovskite phase which may help lead to more stable materials and devices by increasing grain sizes to minimize boundaries,[84, 85] or by finding ligands that can passivate defects at the 2D grain boundaries, similar to how Lewis bases have been shown to passivate surfaces in 3D perovskites.[86]

EXPERIMENTAL METHODS

2D perovskite film fabrication:

Lead iodide (99.999%) and dimethylformamide (99.8% and anhydrous) were purchased from Sigma-Aldrich. n-butylammonium iodide was purchased from Dyesol Ltd. The perovskite precursor solution contains a mixture of 1.0 M tetrabutylammonium iodide and 1.0 M lead iodide in dimethylformamide that was stirred overnight to fully dissolve. Substrates used were glass and indium tin oxide substrates cleaned *via* ultrasonic bath in 2% Micro-90 detergent, deionized water, acetone, and then isopropanol. The glass substrates were dried under nitrogen and then plasma-cleaned for 10 minutes immediately before film deposition. Perovskite films were fabricated by spin-coating 40 μL of precursor solution onto the precleaned substrates at 4000 RPM and 4000 RPM/s for 45 seconds and then annealing for 10 minutes at 70 °C. All steps except the cleaning of glass substrates were performed within a nitrogen-filled glovebox.

AFM measurements:

AFM measurements were performed in the dark for both G-KPFM and FF-trEFM, in both cases on an Asylum Research MFP3D-Bio. G-KPFM data were taken at the Center for Nanophase Materials Science at Oak Ridge National Lab. Pt-coated cantilevers with spring constant ~2 N/m and resonance frequency ~75 kHz were used in both cases. Tips were cleaned with isopropyl alcohol prior to use. For FF-trEFM data the samples were kept under active nitrogen in a sealed flow cell. G-KPFM and FF-trEFM procedures are presented in full detail in their original work.[39, 87] For G-KPFM, the scan rate is set to sample 8.192 ms per pixel, with a typical G-KPFM image as used here being 128 x 64 pixels. The LED is focused *via* a bottom objective on an inverted optical microscopy and co-aligned with the tip. Illumination intensity (per unit area) was measured using a calibrated photodiode and calculating based on a diffraction-limited spot size.

Confocal Microscopy:

We used a custom scanning confocal microscope built around Nikon TE-2000 inverted microscope with 100x infinity corrected dry objective for optical microscopy and spectroscopy. The sample was illuminated with 470 nm pulsed diode laser (PDL-800 LDH-P-C-470B, 1 MHz, ~300 ps pulse width and 9 μJ/cm^2) and the emission was filtered using a 50/50 dichroic beam splitter and a pair of 500 nm long-pass filters. The system was calibrated using 200 nm fluorescent microspheres (Lifetechnologies FluoSpheres Polystyrene Microspheres, 200 nm, red fluorescent, 580/605) prior to measurement. For time-resolved measurements here, the emission was directed to a Micro Photon Devices PDM series single-photon avalanche photodiode with a 50 μm active area and for local-excitation and widefield measurements, the emission was directed to a CCD camera (Pixera, Penguin 150CLM) equipped with a 500 nm long-pass filter. The sample stage was controlled *via* a piezo controller (Physik Instrumente E-710). The pixel size used for fluorescence lifetime images was 100 nm and pixel dwell time (integration time) was 100 ms; the data shown here are 400 x 100 pixels. This setup has been described elsewhere.[53]

Data analysis:

All time-dependent data (both G-KPFM and FF-trEFM) are processed *via* Python scripts interfacing with the Pycroscopy package,[88] with the PyUSID data format.[89] The time-resolved EFM data were converted to Pycroscopy-compatible format and then processed with code used previously.[39, 78] The primary change is the introduction of a Principal Component Analysis (PCA) filtering step prior to the Hilbert transform process, which results in a significant improvement in the quality of the reconstruction. For G-KPFM, the script itself is partially based on code used in F3R and time-resolved EFM.[69, 72] For G-KPFM beyond original F3R is the addition of CPD photocharging time fitting (as proposed in those works). Briefly, we first filter the data for noise related to instrumentation and allow at least the first harmonic in. Then, after accounting for any phase-lag due to voltage reflections and impedance mismatches, we divide the data by the transfer function of the tip as measured previously. We then use PCA to filter extraneous and noisy components of the data that contribute minimally to the variance; typically, the components selected preserve >95% of the variance. At each pixel, we fit the deflection vs. voltage data to a parabola and extract the CPD vs. time as the voltage corresponding to peak (*i.e.* the value $-b/2a$ for a parabola of ax^2+bx+c**)** vs time**.** From the CPD data we then can fit an exponential during illumination to generate photovoltage charging and discharging time maps. Clustering analysis is described in Supplementary Information. The G-KPFM code[90] and the FF-trEFM code[91] are available online.

ACKNOWLEDGMENTS

We acknowledge support from DOE (DOE-SC0013957). J. T. P. is supported by an NSF Graduate Student Fellowship under grant DGE-1256082. S.J. is supported in part by the Clean Energy Institute and National Science Foundation Research Traineeship under award NSF DGE-1633216. This material is based in part upon work supported by the State of Washington through the University of Washington Clean Energy Institute and *via* funding from the Washington Research Foundation. G-Mode KPFM data was conducted at the Center for Nanophase Materials Sciences, which is a DOE Office of Science User Facility.

SUPPORTING INFORMATION AVAILABLE

X-Ray diffraction, additional confocal luminescence data, additional KPFM and CPD data, G-KPFM cross-sections, additional FF-trEFM data and calibration, animated cross-sections of G-KPFM data. This material is available free of charge via the Internet at http://pubs.acs.org.

REFERENCES

1. Stranks, S. D.; Snaith, H. J. Metal-Halide Perovskites for Photovoltaic and Light-Emitting Devices. *Nat. Nanotechnol.* **2015,** *10*, 391-402.
2. Lee, M. M.; Teuscher, J.; Miyasaka, T.; Murakami, T. N.; Snaith, H. J. Efficient Hybrid Solar Cells Based on Meso-Superstructured Organometal Halide Perovskites. *Science* **2012,** *338*, 643-647.
3. Braly, I. L.; deQuilettes, D. W.; Pazos-Outón, L. M.; Burke, S.; Ziffer, M. E.; Ginger, D. S.; Hillhouse, H. W. Hybrid Perovskite Films Approaching the Radiative Limit with over 90% Photoluminescence Quantum Efficiency. *Nature Photonics* **2018,** *12*, 355-361.
4. Fu, W.; Wang, J.; Zuo, L.; Gao, K.; Liu, F.; Ginger, D. S.; Jen, A. K. Y. Two-Dimensional Perovskite Solar Cells with 14.1% Power Conversion Efficiency and 0.68% External Radiative Efficiency. *ACS Energy Lett.* **2018**, 2086-2093.
5. Birkhold, S. T.; Precht, J. T.; Giridharagopal, R.; Eperon, G. E.; Schmidt-Mende, L.; Ginger, D. S. Direct Observation and Quantitative Analysis of Mobile Frenkel Defects in Metal Halide Perovskites Using Scanning Kelvin Probe Microscopy. *J. Phys. Chem. C* **2018,** *122*, 12633-12639.
6. Birkhold, S. T.; Precht, J. T.; Liu, H.; Giridharagopal, R.; Eperon, G. E.; Schmidt-Mende, L.; Li, X.; Ginger, D. S. Interplay of Mobile Ions and Injected Carriers Creates Recombination Centers in Metal Halide Perovskites under Bias. *ACS Energy Lett.* **2018,** *3*, 1279-1286.
7. Yuan, Y.; Huang, J. Ion Migration in Organometal Trihalide Perovskite and Its Impact on Photovoltaic Efficiency and Stability. *Acc. Chem. Res.* **2016,** *49*, 286-293.
8. Cao, D. H.; Stoumpos, C. C.; Farha, O. K.; Hupp, J. T.; Kanatzidis, M. G. 2d Homologous Perovskites as Light-Absorbing Materials for Solar Cell Applications. *J. Am. Chem. Soc.* **2015,** *137*, 7843-7850.
9. Stoumpos, C. C.; Cao, D. H.; Clark, D. J.; Young, J.; Rondinelli, J. M.; Jang, J. I.; Hupp, J. T.; Kanatzidis, M. G. Ruddlesden–Popper Hybrid Lead Iodide Perovskite 2d Homologous Semiconductors. *Chem. Mater.* **2016,** *28*, 2852-2867.
10. Quan, L. N.; Yuan, M.; Comin, R.; Voznyy, O.; Beauregard, E. M.; Hoogland, S.; Buin, A.; Kirmani, A. R.; Zhao, K.; Amassian, A., et al. Ligand-Stabilized Reduced-Dimensionality Perovskites. *J. Am. Chem. Soc.* **2016,** *138*, 2649-2655.
11. Tsai, H.; Nie, W.; Blancon, J. C.; Stoumpos, C. C.; Asadpour, R.; Harutyunyan, B.; Neukirch, A. J.; Verduzco, R.; Crochet, J. J.; Tretiak, S., et al. High-Efficiency Two-Dimensional Ruddlesden-Popper Perovskite Solar Cells. *Nature* **2016,** *536*, 312-6.
12. Smith, I. C.; Hoke, E. T.; Solis-Ibarra, D.; McGehee, M. D.; Karunadasa, H. I. A Layered Hybrid Perovskite Solar-Cell Absorber with Enhanced Moisture Stability. *Angew. Chem. Int. Ed Engl.* **2014,** *126*, 11414-11417.
13. Chen, Y.; Sun, Y.; Peng, J.; Tang, J.; Zheng, K.; Liang, Z. 2d Ruddlesden--Popper Perovskites for Optoelectronics. *Adv. Mater.* **2018,** *30*, 1703487.
14. Straus, D. B.; Kagan, C. R. Electrons, Excitons, and Phonons in Two-Dimensional Hybrid Perovskites: Connecting Structural, Optical, and Electronic Properties. *J. Phys. Chem. Lett.* **2018,** *9*, 1434-1447.
15. Dou, L.; Wong, A. B.; Yu, Y.; Lai, M.; Kornienko, N.; Ginsberg, N. S.; Wang, L.-w.; Alivisatos, A. P.; Yang, P. Atomically Thin Two-Dimensional Organic-Inorganic Hybrid Perovskites. *Science (New York, N.Y.)* **2015,** *349*, 1518-1521.
16. Tsai, H.; Nie, W.; Blancon, J.-C.; Stoumpos, C. C.; Soe, C. M. M.; Yoo, J.; Crochet, J.; Tretiak, S.; Even, J.; Sadhanala, A., et al. Stable Light-Emitting Diodes Using Phase-Pure Ruddlesden-Popper Layered Perovskites. *Adv. Mater.* **2018,** *30*, 1704217.
17. Kumar, S.; Jagielski, J.; Yakunin, S.; Rice, P.; Chiu, Y.-C.; Wang, M.; Nedelcu, G.; Kim, Y.; Lin, S.; Santos, E. J. G., et al. Efficient Blue Electroluminescence Using Quantum-Confined Two-Dimensional Perovskites. *ACS Nano* **2016,** *10*, 9720-9729.
18. Kawano, N.; Koshimizu, M.; Sun, Y.; Yahaba, N.; Fujimoto, Y.; Yanagida, T.; Asai, K. Effects of Organic Moieties on Luminescence Properties of Organic-Inorganic Layered Perovskite-Type Compounds. *J. Phys. Chem. C* **2014,** *118*, 9101-9106.

19. Zhao, T.; Liu, H.; Ziffer, M. E.; Rajagopal, A.; Zuo, L.; Ginger, D. S.; Li, X.; Jen, A. K. Y. Realization of a Highly Oriented Mapbbr3 Perovskite Thin Film Via Ion Exchange for Ultrahigh Color Purity Green Light Emission. *ACS Energy Lett.* **2018,** *3*, 1662-1669.
20. Wu, X.; Trinh, M. T.; Zhu, X. Y. Excitonic Many-Body Interactions in Two-Dimensional Lead Iodide Perovskite Quantum Wells. *J. Phys. Chem. C* **2015,** *119*, 14714-14721.
21. Tanaka, K.; Kondo, T. Bandgap and Exciton Binding Energies in Lead-Iodide-Based Natural Quantum-Well Crystals. *Sci. Technol. Adv. Mater.* **2003,** *4*, 599-604.
22. Hong, X.; Ishihara, T.; Nurmikko, A. V. Dielectric Confinement Effect on Excitons in Pbi4-Based Layered Semiconductors. *Phys. Rev. B Condens. Matter* **1992,** *45*, 6961-6964.
23. Yaffe, O.; Chernikov, A.; Norman, Z. M.; Zhong, Y.; Velauthapillai, A.; van der Zande, A.; Owen, J. S.; Heinz, T. F. Excitons in Ultrathin Organic-Inorganic Perovskite Crystals. *Phys. Rev. B Condens. Matter* **2015,** *92*, 045414.
24. Blancon, J. C.; Stier, A. V.; Tsai, H.; Nie, W.; Stoumpos, C. C.; Traoré, B.; Pedesseau, L.; Kepenekian, M.; Katsutani, F.; Noe, G. T., et al. Scaling Law for Excitons in 2d Perovskite Quantum Wells. *Nat. Commun.* **2018,** *9*, 2254.
25. Ziffer, M. E.; Mohammed, J. C.; Ginger, D. S. Electroabsorption Spectroscopy Measurements of the Exciton Binding Energy, Electron–Hole Reduced Effective Mass, and Band Gap in the Perovskite Ch3nh3pbi3. *ACS Photonics* **2016,** *3*, 1060-1068.
26. Wang, Z.; Lin, Q.; Chmiel, F. P.; Sakai, N.; Herz, L. M.; Snaith, H. J. Efficient Ambient-Air-Stable Solar Cells with 2d–3d Heterostructured Butylammonium-Caesium-Formamidinium Lead Halide Perovskites. *Nature Energy* **2017,** *2*, 17135.
27. deQuilettes, D. W.; Zhang, W.; Burlakov, V. M.; Graham, D. J.; Leijtens, T.; Osherov, A.; Bulović, V.; Snaith, H. J.; Ginger, D. S.; Stranks, S. D. Photo-Induced Halide Redistribution in Organic-Inorganic Perovskite Films. *Nat. Commun.* **2016,** *7*, 11683.
28. Sherkar, T. S.; Momblona, C.; Gil-Escrig, L.; Ávila, J.; Sessolo, M.; Bolink, H. J.; Koster, L. J. A. Recombination in Perovskite Solar Cells: Significance of Grain Boundaries, Interface Traps, and Defect Ions. *ACS Energy Letters* **2017,** *2*, 1214-1222.
29. Yuan, Y.; Chae, J.; Shao, Y.; Wang, Q.; Xiao, Z.; Centrone, A.; Huang, J. Photovoltaic Switching Mechanism in Lateral Structure Hybrid Perovskite Solar Cells. *Adv. En. Mater.* **2015,** *5*, 1500615.
30. Xiao, X.; Dai, J.; Fang, Y.; Zhao, J.; Zheng, X.; Tang, S.; Rudd, P. N.; Zeng, X. C.; Huang, J. Suppressed Ion Migration Along the in-Plane Direction in Layered Perovskites. *ACS Energy Lett.* **2018,** *3*, 684-688.
31. Lin, Y.; Bai, Y.; Fang, Y.; Wang, Q.; Deng, Y.; Huang, J. Suppressed Ion Migration in Low-Dimensional Perovskites. *ACS Energy Lett.* **2017,** *2*, 1571-1572.
32. Tian, H.; Zhao, L.; Wang, X.; Yeh, Y.-W.; Yao, N.; Rand, B. P.; Ren, T.-L. Extremely Low Operating Current Resistive Memory Based on Exfoliated 2d Perovskite Single Crystals for Neuromorphic Computing. *ACS Nano* **2017,** *11*, 12247-12256.
33. Passarelli, J. V.; Fairfield, D. J.; Sather, N. A.; Hendricks, M. P.; Sai, H.; Stern, C. L.; Stupp, S. I. Enhanced out-of-Plane Conductivity and Photovoltaic Performance in N = 1 Layered Perovskites through Organic Cation Design. *J. Am. Chem. Soc.* **2018,** *140*, 7313-7323.
34. Ishihara, T.; Takahashi, J.; Goto, T. Exciton State in Two-Dimensional Perovskite Semiconductor (C10h21nh3)2pbi4. *Solid State Commun.* **1989,** *69*, 933-936.
35. Ishihara, T.; Takahashi, J.; Goto, T. Optical Properties Due to Electronic Transitions in Two-Dimensional Semiconductors (Cnhn+1nh3)2pbi4. *Phys. Rev. B Condens. Matter* **1990,** *42*, 11099-11107.
36. Kagan, C. R.; Mitzi, D. B.; Dimitrakopoulos, C. D. Organic-Inorganic Hybrid Materials as Semiconducting Channels in Thin-Film Field-Effect Transistors. *Science* **1999,** *286*, 945-947.
37. Mitzi, D. B.; Chondroudis, K.; Kagan, C. R. Design, Structure, and Optical Properties of Organic−Inorganic Perovskites Containing an Oligothiophene Chromophore. *Inorg. Chem.* **1999,** *38*, 6246-6256.
38. Coffey, D. C.; Ginger, D. S. Time-Resolved Electrostatic Force Microscopy of Polymer Solar Cells. *Nature materials* **2006,** *5*, 735-40.

39. Giridharagopal, R.; Rayermann, G. E.; Shao, G.; Moore, D. T.; Reid, O. G.; Tillack, A. F.; Masiello, D. J.; Ginger, D. S. Submicrosecond Time Resolution Atomic Force Microscopy for Probing Nanoscale Dynamics. *Nano Lett.* **2012,** *12*, 893-8.
40. Cox, P. A.; Glaz, M. S.; Harrison, J. S.; Peurifoy, S. R.; Coffey, D. C.; Ginger, D. S. Imaging Charge Transfer State Excitations in Polymer/Fullerene Solar Cells with Time-Resolved Electrostatic Force Microscopy. *J. Phys. Chem. Lett.* **2015,** *6*, 2852-2858.
41. Shao, G.; Rayermann, G. E.; Smith, E. M.; Ginger, D. S. Morphology-Dependent Trap Formation in Bulk Heterojunction Photodiodes. *Journal of Physical Chemistry B* **2013,** *117*, 4654-4660.
42. Reid, O. G.; Rayermann, G. E.; Coffey, D. C.; Ginger, D. S. Imaging Local Trap Formation in Conjugated Polymer Solar Cells: A Comparison of Time-Resolved Electrostatic Force Microscopy and Scanning Kelvin Probe Imaging. *The Journal of Physical Chemistry C* **2010,** *114*, 20672-20677.
43. Harrison, J. S.; Waldow, D. A.; Cox, P. A.; Giridharagopal, R.; Adams, M.; Richmond, V.; Modahl, S.; Longstaff, M.; Zhuravlev, R.; Ginger, D. S. Noncontact Imaging of Ion Dynamics in Polymer Electrolytes with Time-Resolved Electrostatic Force Microscopy. *ACS Nano* **2018,** *10.1021/acsnano.8b07254*.
44. Dwyer, R. P.; Nathan, S. R.; Marohn, J. A. Microsecond Photocapacitance Transients Observed Using a Charged Microcantilever as a Gated Mechanical Integrator. *Science Advances* **2017,** *3*, e1602951.
45. Kalinin, S. V.; Strelcov, E.; Belianinov, A.; Somnath, S.; Vasudevan, R. K.; Lingerfelt, E. J.; Archibald, R. K.; Chen, C.; Proksch, R.; Laanait, N., et al. Big, Deep, and Smart Data in Scanning Probe Microscopy. *ACS Nano* **2016,** *10*, 9068-9086.
46. Umebayashi, T.; Asai, K.; Kondo, T.; Nakao, a. Electronic Structures of Lead Iodide Based Low-Dimensional Crystals. *Physical Review B* **2003,** *67*, 2-7.
47. Zhao, Y.-Q.; Ma, Q.-R.; Liu, B.; Yu, Z.-L.; Yang, J.; Cai, M.-Q. Layer-Dependent Transport and Optoelectronic Property in Two-Dimensional Perovskite: (Pea)2pbi4. *Nanoscale* **2018,** *10*, 8677-8688.
48. Zhang, Q.; Chu, L.; Zhou, F.; Ji, W.; Eda, G. Excitonic Properties of Chemically Synthesized 2d Organic--Inorganic Hybrid Perovskite Nanosheets. *Adv. Mater.* **2018**, 1704055.
49. Soe, C. M. M.; Stoumpos, C. C.; Kepenekian, M.; Traoré, B.; Tsai, H.; Nie, W.; Wang, B.; Katan, C.; Seshadri, R.; Mohite, A. D., et al. New Type of 2d Perovskites with Alternating Cations in the Interlayer Space, (C(Nh2)3)(Ch3nh3)Npbni3n+1: Structure, Properties, and Photovoltaic Performance. *J. Am. Chem. Soc.* **2017,** *139*, 16297-16309.
50. Wang, J.; Li, J.; Tan, Q.; Li, L.; Zhang, J.; Zang, J.; Tan, P.; Zhang, J.; Li, D. Controllable Synthesis of Two-Dimensional Ruddlesden–Popper-Type Perovskite Heterostructures. *J. Phys. Chem. Lett.* **2017,** *8*, 6211-6219.
51. Blancon, J. C.; Tsai, H.; Nie, W.; Stoumpos, C. C.; Pedesseau, L.; Katan, C.; Kepenekian, M.; Soe, C. M. M.; Appavoo, K.; Sfeir, M. Y., et al. Extremely Efficient Internal Exciton Dissociation through Edge States in Layered 2d Perovskites. *Science* **2017,** *355*, 1288-1292.
52. Milot, R. L.; Sutton, R. J.; Eperon, G. E.; Haghighirad, A. A.; Martinez Hardigree, J.; Miranda, L.; Snaith, H. J.; Johnston, M. B.; Herz, L. M. Charge-Carrier Dynamics in 2d Hybrid Metal–Halide Perovskites. *Nano Lett.* **2016,** *16*, 7001-7007.
53. deQuilettes, D. W.; Jariwala, S.; Burke, S.; Ziffer, M. E.; Wang, J. T. W.; Snaith, H. J.; Ginger, D. S. Tracking Photoexcited Carriers in Hybrid Perovskite Semiconductors: Trap-Dominated Spatial Heterogeneity and Diffusion. *ACS Nano* **2017,** *11*, 11488-11496.
54. Stranks, S. D.; Eperon, G. E.; Grancini, G.; Menelaou, C.; Alcocer, M. J. P.; Leijtens, T.; Herz, L. M.; Petrozza, A.; Snaith, H. J. Electron-Hole Diffusion Lengths Exceeding 1 Micrometer in an Organometal Trihalide Perovskite Absorber. *Science (New York, N.Y.)* **2013,** *342*, 341-344.
55. Kronik, L.; Shapira, Y. Surface Photovoltage Phenomena: Theory, Experiment, and Applications. *Surface Science Reports* **1999,** *37*, 1-206.
56. Barnea-Nehoshtan, L.; Kirmayer, S.; Edri, E.; Hodes, G.; Cahen, D. Surface Photovoltage Spectroscopy Study of Organo-Lead Perovskite Solar Cells. *J. Phys. Chem. Lett.* **2014,** *5*, 2408-2413.
57. Park, Y.; Choong, V.; Gao, Y.; Hsieh, B. R.; Tang, C. W. Work Function of Indium Tin Oxide Transparent Conductor Measured by Photoelectron Spectroscopy. *Appl. Phys. Lett.* **1996,** *68*, 2699-2701.

58. Kim, J. S.; Lägel, B.; Moons, E.; Johansson, N.; Baikie, I. D.; Salaneck, W. R.; Friend, R. H.; Cacialli, F. Kelvin Probe and Ultraviolet Photoemission Measurements of Indium Tin Oxide Work Function: A Comparison. *Synthetic Metals* **2000,** *111-112*, 311-314.
59. Silver, S.; Yin, J.; Li, H.; Brédas, J.-L.; Kahn, A. Characterization of the Valence and Conduction Band Levels of N = 1 2d Perovskites: A Combined Experimental and Theoretical Investigation. *Adv. Energy Mater.* **2018,** *8*, 1703468.
60. Nagaoka, H.; Ma, F.; Dequilettes, D. W.; Vorpahl, S. M.; Glaz, M. S.; Colbert, A. E.; Ziffer, M. E.; Ginger, D. S. Zr Incorporation into Tio2 Electrodes Reduces Hysteresis and Improves Performance in Hybrid Perovskite Solar Cells While Increasing Carrier Lifetimes. *J. Phys. Chem. Lett.* **2015,** *6*, 669-675.
61. Moerman, D.; Kim, H.; Colbert, A. E.; Graham, S.; Ginger, D. S. The Impact of Ultra-Thin Titania Interlayers on Open Circuit Voltage and Carrier Lifetime in Thin Film Solar Cells. *App. Phys. Lett.* **2016,** *108*, 113301.
62. Mahmood, K.; Sarwar, S.; Mehran, M. T. Current Status of Electron Transport Layers in Perovskite Solar Cells: Materials and Properties. *RSC Adv.* **2017,** *7*, 17044-17062.
63. Garrett, J. L.; Munday, J. N. Fast, High-Resolution Surface Potential Measurements in Air with Heterodyne Kelvin Probe Force Microscopy. *Nanotechnology* **2016,** *27*, 245705.
64. Garrett, J. L.; Tennyson, E. M.; Hu, M.; Huang, J.; Munday, J. N.; Leite, M. S. Real-Time Nanoscale Open-Circuit Voltage Dynamics of Perovskite Solar Cells. *Nano Lett* **2017,** *17*, 2554-2560.
65. Tennyson, E. M.; Garrett, J. L.; Frantz, J. A.; Myers, J. D.; Bekele, R. Y.; Sanghera, J. S.; Munday, J. N.; Leite, M. S. Nanoimaging of Open-Circuit Voltage in Photovoltaic Devices. *Adv. En. Mater.* **2015,** *5*, 1501142.
66. Bergmann, V. W.; Guo, Y.; Tanaka, H.; Hermes, I. M.; Li, D.; Klasen, A.; Bretschneider, S. A.; Nakamura, E.; Berger, R.; Weber, S. A. L. Local Time-Dependent Charging in a Perovskite Solar Cell. *ACS Appl. Mater. Interfaces* **2016**.
67. Collins, S. D.; Mikhnenko, O. V.; Nguyen, T. L.; Rengert, Z. D.; Bazan, G. C.; Woo, H. Y.; Nguyen, T.-Q. Observing Ion Motion in Conjugated Polyelectrolytes with Kelvin Probe Force Microscopy. *Adv. Electron. Mater.* **2017,** *3*, 1700005.
68. Tirmzi, A. M.; Dwyer, R. P.; Hanrath, T.; Marohn, J. A. Coupled Slow and Fast Charge Dynamics in Cesium Lead Bromide Perovskite. *ACS Energy Letters* **2017,** *2*, 488-496.
69. Collins, L.; Ahmadi, M.; Qin, J.; Liu, Y.; Ovchinnikova, O. S.; Hu, B.; Jesse, S.; Kalinin, S. V. Time Resolved Surface Photovoltage Measurements Using a Big Data Capture Approach to Kpfm. *Nanotechnology* **2018,** *29*, 445703.
70. Belianinov, A.; Kalinin, S. V.; Jesse, S. Complete Information Acquisition in Dynamic Force Microscopy. *Nat. Commun.* **2015,** *6*, 6550.
71. Collins, L.; Belianinov, A.; Somnath, S.; Balke, N.; Kalinin, S. V.; Jesse, S. Full Data Acquisition in Kelvin Probe Force Microscopy: Mapping Dynamic Electric Phenomena in Real Space. *Sci. Rep.* **2016,** *6*, 30557.
72. Collins, L.; Ahmadi, M.; Wu, T.; Hu, B.; Kalinin, S. V.; Jesse, S. Breaking the Time Barrier in Kelvin Probe Force Microscopy: Fast Free Force Reconstruction Using the G-Mode Platform. *ACS Nano* **2017,** *11*, 8717-8729.
73. Schumacher, Z.; Miyahara, Y.; Spielhofer, A.; Grutter, P. Measurement of Surface Photovoltage by Atomic Force Microscopy under Pulsed Illumination. *Phys. Rev. Applied* **2016,** *5*, 044018.
74. Gélvez-Rueda, M. C.; Hutter, E. M.; Cao, D. H.; Renaud, N.; Stoumpos, C. C.; Hupp, J. T.; Savenije, T. J.; Kanatzidis, M. G.; Grozema, F. C. Interconversion between Free Charges and Bound Excitons in 2d Hybrid Lead Halide Perovskites. *J. Phys. Chem. C Nanomater. Interfaces* **2017,** *121*, 26566-26574.
75. Delugas, P.; Caddeo, C.; Filippetti, A.; Mattoni, A. Thermally Activated Point Defect Diffusion in Methylammonium Lead Trihalide: Anisotropic and Ultrahigh Mobility of Iodine. *The Journal of Physical Chemistry Letters* **2016,** *7*, 2356-2361.

76. Kumar, M.; Kim, H. S.; Park, D. Y.; Jeong, M. S.; Kim, J. Compliance-Free Multileveled Resistive Switching in a Transparent 2d Perovskite for Neuromorphic Computing. *ACS Appl Mater Interfaces* **2018,** *10*, 12768-12772.
77. Belianinov, A.; Vasudevan, R.; Strelcov, E.; Steed, C.; Yang, S. M.; Tselev, A.; Jesse, S.; Biegalski, M.; Shipman, G.; Symons, C., et al. Big Data and Deep Data in Scanning and Electron Microscopies: Deriving Functionality from Multidimensional Data Sets. *Advanced Structural and Chemical Imaging* **2015,** *1*, 6.
78. Karatay, D. U.; Harrison, J. S.; Glaz, M. S.; Giridharagopal, R.; Ginger, D. S. Fast Time-Resolved Electrostatic Force Microscopy: Achieving Sub-Cycle Time Resolution. *Review of Scientific Instruments* **2016,** *87*, 053702.
79. Dwyer, R. P.; Harrell, L. E.; Marohn, J. A. Lagrangian and Impedance Spectroscopy Treatments of Electric Force Microscopy. *arXiv [cond-mat.mes-hall]* **2018**.
80. Peng, W.; Yin, J.; Ho, K.-T.; Ouellette, O.; De Bastiani, M.; Murali, B.; El Tall, O.; Shen, C.; Miao, X.; Pan, J., et al. Ultralow Self-Doping in Two-Dimensional Hybrid Perovskite Single Crystals. *Nano Lett.* **2017,** *17*, 4759-4767.
81. Li, C.; Wan, J.; Zheng, Y.; Dong, W. Tuning Photoconductive Properties of Organic–Inorganic Hybrid Perovskite Nanocomposite Device Via Organic Layer's Thickness. *Mater. Lett.* **2012,** *76*, 187-189.
82. Kutes, Y.; Zhou, Y.; Bosse, J. L.; Steffes, J.; Padture, N. P.; Huey, B. D. Mapping the Photoresponse of Ch3nh3pbi3 Hybrid Perovskite Thin Films at the Nanoscale. *Nano Lett.* **2016,** *16*, 3434-3441.
83. Bonnell, D. A.; Kalinin, S. V., *Scanning Probe Microscopy for Energy Research*. World Scientific: New Jersey, 2103; Vol. 7.
84. DeQuilettes, D. W.; Vorpahl, S. M.; Stranks, S. D.; Nagaoka, H.; Eperon, G. E.; Ziffer, M. E.; Snaith, H. J.; Ginger, D. S. Impact of Microstructure on Local Carrier Lifetime in Perovskite Solar Cells. *Science* **2015,** *348*, 683-686.
85. Nie, W.; Tsai, H.; Asadpour, R.; Blancon, J.-C.; Neukirch, A. J.; Gupta, G.; Crochet, J. J.; Chhowalla, M.; Tretiak, S.; Alam, M. A., et al. High-Efficiency Solution-Processed Perovskite Solar Cells with Millimeter-Scale Grains. *Science* **2015,** *347*, 522.
86. deQuilettes, D. W.; Koch, S.; Burke, S.; Paranji, R. K.; Shropshire, A. J.; Ziffer, M. E.; Ginger, D. S. Photoluminescence Lifetimes Exceeding 8 Ms and Quantum Yields Exceeding 30% in Hybrid Perovskite Thin Films by Ligand Passivation. *ACS Energy Letters* **2016,** *1*, 438-444.
87. Collins, L.; Belianinov, A.; Somnath, S.; Rodriguez, B. J.; Balke, N.; Kalinin, S. V.; Jesse, S. Multifrequency Spectrum Analysis Using Fully Digital G Mode-Kelvin Probe Force Microscopy. *Nanotechnology* **2016,** *27*, 105706.
88. Somnath, Suhas, Chris R. Smith, Nouamane Laanait, and Stephen Jesse. Pycroscopy. Computer software. Vers. 0.60.0. Oak Ridge National Laboratory, 01 June 2016. Web. <https://pycroscopy.github.io/pycroscopy/about.html>.
89. Somnath, Suhas, Chris R. Smith, and Stephen Jesse. pyUSID. Computer software. Vers. 0.0.4. Oak Ridge National Laboratory, 01 June 2018. Web. <https://pycroscopy.github.io/pyUSID/about.html>
90. https://github.com/rajgiriUW/GKPFM
91. https://bitbucket.org/gingerlab/ffta/overview